F. Ornati, P. Panicucci, A. Pizzetti, F. Capolupo, F. Topputo
On the Radiometric Calibration of Optical Hardware-in-the-Loop Stimulators
Journal of Spacecraft and Rockets, published online 22/04/2026
doi:10.2514/1.a36543

On the Radiometric Calibration of Optical Hardware-In-the-Loop Stimulators

Fabio Ornati*, Paolo Panicucci†, Andrea Pizzetti‡
Politecnico di Milano, Via La Masa 34, 20156, Milan, Italy

Francesco Capolupo§
European Space Agency, ESA, Keplerlaan 1, 2201 AZ Noordwijk, Netherlands

Francesco Topputo¶
Politecnico di Milano, Via La Masa 34, 20156, Milan, Italy

Optical stimulators are essential for performing validation and verification of spaceborne optical systems, allowing realistic, hardware-in-the-loop testing under controlled conditions. These facilities bridge the domain gap between synthetic image rendering and real mission data, ensuring a close-to-real evaluation of image processing algorithm performance. An open challenge in their use is the reproduction of radiometric-equivalent images that faithfully replicate in-space acquisitions. This work presents a detailed methodology for the radiometric calibration of optical stimulators, enabling the high-fidelity emulation of both resolved and pointwise objects. The proposed methodology is applied to two different testbeds and validated using an industrial camera and a high-TRL star tracker. Experimental results demonstrate the accuracy of the proposed framework in reproducing realistic scenes, including detailed hardware-specific optical effects that are often beyond the scope of conventional rendering tools.

Nomenclature

f_c	=	collimator focal lenght
μ_s	=	screen pixel pitch
θ_{FoV}	=	angular field-of-view
h_r	=	radial distance on the screen
θ	=	inclination of collimated rays
φ	=	inclination of chief ray
d	=	distance between camera collimator and camera pupil

*Ph.D. Student, Department of Aerospace Science and Technology, fabio.ornati@polimi.it.
†Assistant Professor, Department of Aerospace Science and Technology.
‡Ph.D. Student, Department of Aerospace Science and Technology.
§GNC Systems Engineer, Guidance, Navigation and Control Section
¶Full Professor, Department of Aerospace Science and Technology, AIAA Senior Member

B = digital count

A_p = pupil area

P = radiant flux

$I_\Omega(\varphi)$ = radiant intensity

ω = projected solid angle

L_0 = pixel radiance

λ = wavelength

$S(\lambda)$ = power sensor sensitivity

I_m = measured current

P_m = measured radiant power

$\hat{P}_\lambda(\lambda)$ = screen relative spectral distribution

k_P = spectral distribution scaling factor

A_m = power sensor aperture area

P_{e^-} = electron flux

h = Planck's constant

c = light speed in vacuum

$\eta(\lambda)$ = normalized camera response curve

$Q(\lambda)$ = camera sensor quantum efficiency

$T(\lambda)$ = objective lens transmissivity

F_λ = radiant flux density

$F_{\text{eff}}^{(r)}$ = rendering predicted effective radiant flux density

$F_{\text{eff}}^{(h)}(B)$ = facility emulated effective radiant flux density

m_X = apparent magnitude of the generic X photometric filter

F_X = radiant flux density of the generic X photometric filter

$X(\lambda)$ = relative transmissivity of the generic X photometric filter

$M_{BB}(\lambda)$ = black body spectral exitance

K_B = Boltzmann constant

T_{eff} = effective star temperature

I. Introduction

Optical devices are indispensable tools in space exploration, as they provide critical data for a wide array of applications. These devices are omnipresent onboard spacecraft: scientific cameras are important payloads used to

image the surface of celestial bodies, navigation cameras are used to perform optical navigation, and star trackers process images of the starry sky to determine the spacecraft attitude. Optical cameras have become the state of the art to ensure reliable and accurate measurements for autonomous navigation systems. Multiple authors have proposed Image Processing (IP) algorithms for Vision-based navigation (VBN) with applicative scenarios involving celestial bodies at different ranges. These include celestial triangulation algorithms that exploit far-range planets as navigation beacons [1–3], medium-range applications that use the limb or the apparent diameter of observed planets [4–6], and close-range algorithms based upon local feature tracking [7] and terrain relative navigation (TRN). Additionally, Convolutional Neural Networks (CNN) and other data-driven IP algorithms are being experimented with as a possible way of extracting information to obtain more accurate navigation solutions [8, 9].

Due to the increasingly critical role of vision-based algorithms throughout all the phases of a mission, detailed testing and validation processes must be put in place to evaluate their performance and to verify their correct implementation and interface within hardware components. To achieve these goals, a vast amount of realistic and diverse images with associated ground truth information is essential for achieving the desired validation confidence. These images can be retrieved by three different sources. The first source consists of real mission datasets. These are the most realistic and accurate, as they are obtained directly from previously flown space missions. However, they are limited in number and diversity of scenarios, and their reference values are inherently affected by orbit determination errors [10]. The second source consists of rendered images, which are synthetically generated aiming to achieve the same fidelity of the real scenarios with dedicated software. These images are immune to ground truth errors and allow complete freedom in the scenario reproduction. However, this technique requires accurate modeling of the optical and radiometric characteristics of the imaging device. The technique also requires precise knowledge of the radiometric properties of the objects in the scene (e.g., reflectivity, color, albedo) and how they interact with each other and the camera. These complex modelling requirements become especially relevant when simulating phenomena occurring out of the nominal operating envelope of the camera (e.g., saturation, stray light, aberrations, etc.), which are inherently difficult to characterize and replicate accurately.

The third approach consists of Hardware-In-The-loop (HIL) test. In this case, the images are acquired through real hardware equipment stimulated by a testing facility. The facility emulates the visual conditions of real space scenarios, thus ensuring a realistic response of the imaging system. Notably, this approach requires a simpler rendering pipeline, avoiding the need to apply specific optical effects since these are intrinsically deriving from the hardware itself. This approach is admittedly the most complex of the three, due to the inherent challenges in integrating software tools, hardware components, and calibration algorithms. It is, however, a valid alternative as it allows validating the integrated imaging system together with the underlying software, enabling the identification of unforeseen behaviors in the interaction between the two.

The increasing interest in optical stimulation is demonstrated by the significant number of new facility designs

presented in literature. These testbeds have been used to test and validate various kinds of attitude determination and navigation algorithms. Among former examples is the one presented in [11] in 2001. The testbed, purposed at the stimulation of star trackers, consists of two main components: a screen onto which the starfield images are displayed and a collimator lens to project the optical scene at infinity. The star tracker head is mounted behind the collimator and all the equipment is enclosed in a dark room to eliminate external light interferences. The same overall architecture, with substantial variations in the sizes and the technological maturity of the components, can be found in all of the subsequent literature examples [12–18]. In [19], a new design characterized by the presence of multiple movable lenses is introduced. This architecture is able to achieve variable magnification, thus enabling the use of cameras with different characteristics without the need to redesign the facility. This feature is achieved by adjusting the relative position of the lenses.

The Deep-Space Astrodynamics Research and Technology (DART) group at Politecnico di Milano developed two of these facilities in the past years, TinyV3RSE [20] and RETINA [21]. The former is a fixed-magnification testbed designed to host medium-sized cameras and star trackers in close- and medium-range HIL navigation tests. The latter is a variable magnification facility able to host a broad range of narrow Field-of-View (FoV) cameras. RETINA is used in the context of the ERC-funded EXTREMA project [22] as the main optical facility of the EXTREMA Simulation Hub (ESH) [23] to emulate the visual conditions met by a CubeSat during a deep-space transfer cruise [24].

The calibration of the optical stimulators is fundamental for their utilization. A facility must be characterized and calibrated both geometrically and radiometrically to generate realistic scenes. The geometric calibration defines the projection model of the facility, that is, a mapping between the geometrical Line-of-Sight (LoS) detected by the camera and the corresponding pixel positions on the screen. This mapping allows the reproduction of the geometric characteristics of the virtual scenes, thus correcting the optical distortions induced by the collimating optics and the misalignment between the components. Several geometric calibration strategies have been discussed in the literature. Among these, the ones in [14] and [16] are based upon polynomials, while the one in [15] uses the classic camera projection model coupled with radial and tangential distortion coefficients.

The radiometric calibration, instead, is essential to accurately emulate the intensity of the virtual scenes and the pixel content of the image. In practice, the calibration establishes a mapping between the digital count of pixels of the screen and the corresponding radiometric intensity perceived by the deployed camera. Since the scenes may involve objects at various ranges, the radiometric calibration procedure must be able to handle both resolved and unresolved objects. Overall, radiometric fidelity is a key requirement to generate images that are as close as possible to real counterparts. This aspect is fundamental to observe and validate the behaviour and performance of image processing algorithms, which are strongly influenced by even small variations in radiometric conditions. In particular, geometric outputs such as computed locations of centroids, limbs, and features in the images may differ from the intended ones in the case of imprecise calibration. Likewise, absolute radiometric accuracy is paramount in the case of dim objects, for which the

recognizability is predominantly influenced by their brightness. This is the case of scenarios involving asteroids and artificial satellites approached from a far distance [25]. Calibration accuracy becomes also critical in the presence of highly non-linear, sensor-specific effects (such as saturation, blooming, and charge bleeding) that can substantially alter the visual characteristics of the image. As can be evinced from these needs, the radiometric emulation process must not only replicate relative intensity variations but also accurately reproduce the absolute magnitude of these effects with high fidelity.

Any of the mentioned effects on IP outputs could negatively affect the validation confidence of the HIL setup, potentially undermining future space missions that leverage those algorithms. In the past, the lack of on-ground validation and test capabilities has impacted multiple missions. For example, the AVANTI experiment [26] experienced degraded star detectability due to an overly bright target, while NASA's Artemis I OpNav camera suffered from incorrect exposure settings during its first lunar passage [27].

Despite the evidenced importance, only a few HIL facilities in the literature define a clear radiometric calibration procedure. Some of them only focus on achieving geometric fidelity [15] and others are solely based upon the parameters stated by the screen manufacturers [11, 17]. A step toward radiometric realism can be found in [16], which presents a procedure based upon external independent measurements. The authors used a commercial light power meter to measure the irradiance produced by the screen at various digital count levels.

The main contribution of this work is to provide a clear and detailed procedure for emulating the radiometric properties of both resolved and pointwise objects in optical HIL stimulators. The procedure considers the spectral distribution of the light emitted by the screen and the spectral sensitivity of the camera under testing to improve the fidelity of the emulation process. The accuracy and consistency of the emulation procedure are validated quantitatively against real night-sky images and high-fidelity images rendered with a physically-based renderer. The proposed methodology is applied in RETINA and TinyV3RSE and tested with both a space-graded star tracker and an industrial camera for computer vision applications. The tests are conducted under varying exposure conditions to assess performance across diverse scenarios.

The remainder of this paper is structured as follows. Section II discusses the radiometric modeling of a typical optical HIL stimulator. This section also describes the calibration measurements acquisition and the procedure to achieve the same camera response of real scenarios. The emulation procedure is specialized in the cases of pointwise and resolved objects. Then, Section III focuses on the validation of the developed framework using real hardware. Conclusions are drawn in Section IV.

II. Theoretical framework

A. Opto-geometric model of optical HIL stimulators

Optical HIL facilities are designed to stimulate cameras in a way that makes them output images akin to those acquired in orbit. This process requires at least two hardware components: a screen and a correcting lens system. The overall architecture of a facility and its components are schematized in Fig. 1a and 1b for fixed magnification and variable magnification setups, respectively.

The screen serves as the primary interface for displaying rendered synthetic scenes within the optical stimulator. However, because its surface is composed of discrete pixels, it can only approximate the continuous nature of real-world environments through a discretized representation. This introduces inherent limitations in the geometrical accuracy of the scenes. To mitigate these effects, screens are typically chosen to provide the highest resolution possible.

The correcting lens system is used to achieve optical collimation. In this way, the scene displayed on the screen at a

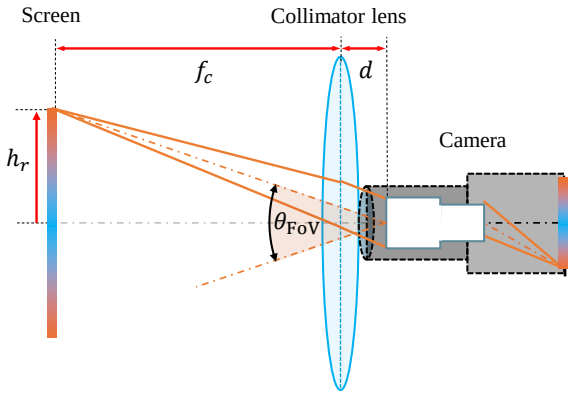

(a) Fixed mangnification

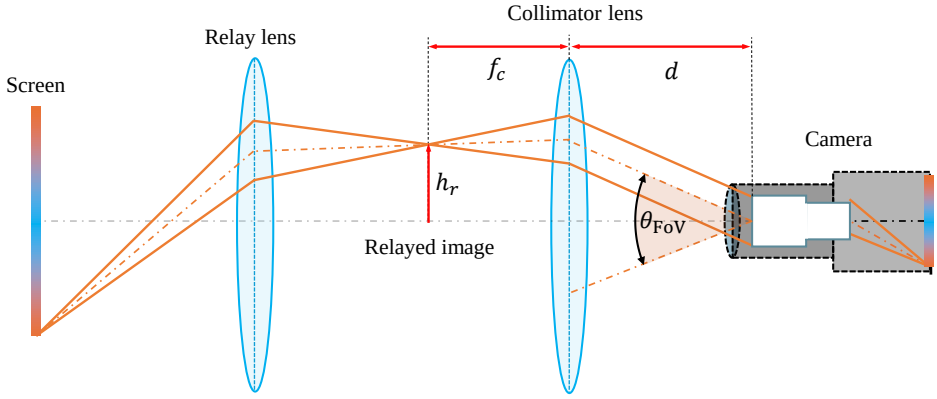

(b) Variable mangnification

Fig. 1 Architecture and components of fixed (a) and variable (b) magnification optical stimulators.

finite distance appears to the camera as if it were located at infinity. This is accomplished, in the case of single-lens facilities, by positioning the lens exactly one focal length away from the display. This imposes strict constraints in the selection of the collimator focal length f_c as it must ensure that the camera FoV aligns precisely with the physical dimensions of the screen [11]. The optimal matching condition, for which the camera observes the whole screen and no pixels are outside of its FoV is obtained by selecting a lens with a focal length f_c such that:

$$f_c = \frac{2\mu_s N_v}{\tan\left(\frac{\theta_{\text{FoV}}}{2}\right)} \tag{1}$$

where μ_s and N_v are the screen pixel pitch and resolution, respectively, and θ_{FoV} is the camera FoV angle.

In the case of variable-magnification testbeds, the screen is magnified by an additional lens - named relay lens - as shown in Fig. 1b. In this case, a virtual image is formed between the two lenses, which is then collimated to stimulate the optical sensor. By adjusting the position of the relay lens, the size of the virtual image is modified, thereby altering the magnification of the optical system to fit the camera FoV. This flexibility allows the matching condition to be achieved across a wide range of camera FoVs without requiring the selection of a specific lens model for each camera-screen combination [19].

As shown in the bi-dimensional sketch in Fig. 1a, the rays originating from a given pixel position of the screen become collimated after the collimator lens. This means that each screen pixel of the screen produces light in a specific range of angular directions. A given point on the screen at radial distance h_r from the boresight axis is associated with rays with inclination θ that can be computed as [20]:

$$\theta = \arctan\left(\frac{h_r}{f_c}\right) \tag{2}$$

In the case of variable magnification stimulators, the radial distance h_r is the one related to the virtual image, which is scaled by the magnification factor M. For the sake of simplicity, the following equations will only consider single-lens facilities since the same relations derived for the screen can be referred to its virtual magnified image in the case of multiple-lens facilities. As shown in Figure 2, the inclination angle φ of the chief ray (dot-dashed lines) when departing the screen (or the virtual image) can be computed by exploiting the properties of thin lenses:

$$\varphi = \arctan\left(\frac{h_r - d\tan(\theta)}{f_c}\right) = \arctan\left(\frac{h_r}{f_c}\left(1 - \frac{d}{f_c}\right)\right) \tag{3}$$

where d is the distance between the camera entrance pupil and the collimator lens. It is worth noting that $\varphi = \theta$ when the camera pupil coincides with the collimator lens and $\varphi = 0$ when the camera pupil is one focal length f_c away from the collimator.

Note that Eqs. (2) and (3) can be considered first-order approximations that are valid in the case of perfect alignment between the optical components and in the absence of optical distortions and aberrations. In reality these conditions are never met, therefore a more refined model is required to effectively relate the screen coordinates and the direction of the light after the collimator lens. This mapping is expressed through the geometric calibration procedure, which defines the actual projection model of the facility. The geometric calibration can be characterized using one of the several methodologies presented in the literature, which usually involve the acquisition of calibration patterns on the screen with known geometric characteristics [15, 20, 21].

B. Radiometric model of optical HIL stimulators

Radiometric modeling of the facility is crucial for understanding how the camera is stimulated. The purpose of this section is to investigate and understand how the light generated by the screen is transmitted to the camera sensor. In particular, the following equations aim to establish a relation between a known property of the screen - the radiance of each pixel as a function of the digital count B - and the emulated radiant flux density experienced at the camera pupil.

Figure 2 shows the schematized viewing geometry of a typical optical stimulator. All the components are assumed to be perfectly aligned, with the lens parallel to the screen plane and perpendicular to the camera boresight. The camera, whose pupil aperture area is $A_p = \pi \left(\frac{d_p}{2}\right)^2$, collects the light emitted by the screen. For a given pointwise emitter on the screen having a radiant intensity $I_\Omega(\varphi)$, the radiant flux P reaching the sensor can be computed as:

$$P = I_\Omega(\varphi)\ \omega(\varphi) \tag{4}$$

where $\omega(\varphi) = \Omega(\varphi)\cos(\varphi)$ is the projected solid angle associated with the camera pupil that collects light within the solid angle $\Omega(\varphi)$ [28]. The exact value of this quantity can be only computed numerically [29], however, it can be reasonably approximated for small pupil-diameter-to-focal-length ratios as:

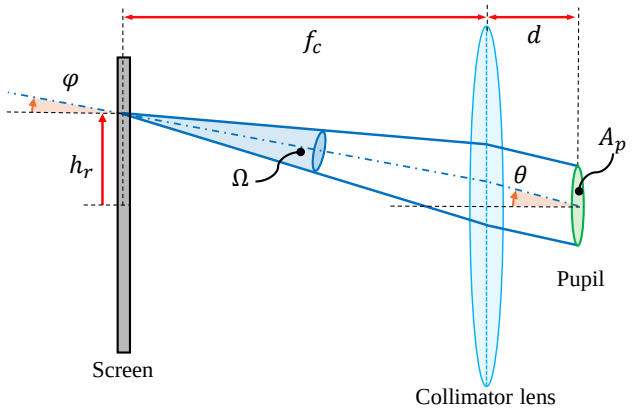

Fig. 2 Viewing geometry scheme of a single lens facility.

$$\omega(\varphi) = \Omega(\varphi)\cos(\varphi) = \frac{A_p}{\left(\frac{f_c}{\cos(\varphi)}\right)^2}\cos(\varphi) = \frac{A_p\cos^3(\varphi)}{f_c^2} \tag{5}$$

In the case of a Lambertian emitter, the radiant intensity can be expressed using the classic Lambert's cosine law [28]:

$$I_\Omega = I_0\cos(\varphi) \tag{6}$$

where I_0 is the radiant intensity in the direction perpendicular to the emitting surface. Note that I_0 is a lumped property since the pixel is not a pointwise emitter but is characterized by an extended surface. In particular, the radiant intensity I_0 is computed by integrating the radiance of the pixel $L_0(B,\varphi)$ over its surface $A_s = \mu_s^2$ [28]:

$$I_0(B) = \oint_{A_s} L_0(B,\varphi)\, dA_s \tag{7}$$

The directional dependence of the radiance L_0 can be neglected within the assumption of a Lambertian emitter. However, in practice, the value of L_0 is not homogeneous across the pixel since each of these is generally composed of at least three sub-pixel matrices with varying characteristics, including dark areas that do not emit light. Alternatively, an average value of radiance $\bar{L}_0(B)$ can be considered, for which:

$$I_0(B) = \bar{L}_0(B)A_s \tag{8}$$

At this point, the radiant flux density $F(B)$ reproduced by the facility at the camera pupil can be computed by dividing the radiant power P of Eq. (4) by the projected pupil area:

$$F(B) = \frac{P(B)}{A_p\cos(\varphi)} = \frac{\bar{L}_0(B)A_s\cos^3(\varphi)}{f_c^2} \tag{9}$$

Equation (9) expresses the radiant flux density produced by a single pixel on the screen as a function of its radiance. Note that the value of the radiance is a controllable quantity function of the pixel digital count B. Therefore, if the $\bar{L}_0(B)$ relation is known, it is possible to invert Eq. (9) to find the closest screen digital count level B for representing a given radiant flux density value. This strategy is essentially the one followed by [13] for reproducing stellar objects in HIL tests.

Note that the prediction of the radiant flux density value using this procedure, based only upon modeling, may be inaccurate due to relatively high uncertainties in the components of Eq. (9) and the presence of additional unmodeled effects (e.g., screen anisotropies). It is also worth highlighting that this simplified formulation leverages multiple assumptions, such as the Lambertian emittivity and extended properties lumping. Moreover, Eq. (9) does not include

any term related to the transmissivity of the optical system, potentially neglecting relevant levels of attenuation in the case of facilities with multiple lenses. The $\bar{L}_0(B)$ Look-Up Table (LUT) is rarely disclosed by screen manufacturers, which often only state the maximum radiance value expressed in terms of luminance. This has forced other authors [17] to use an approximate LUT obtained by scaling the maximum radiance $\bar{L}_0^{\max}$ according to the gamma correction value γ stated for the screen:

$$\bar{L}_0(B) = \bar{L}_0^{\max} \left(\frac{B}{2^n - 1} \right)^{\gamma} \tag{10}$$

where n is the bit depth of the controlled screen intensity.

In addition to these factors, the actual value of radiance could be affected by several other sources of uncertainty, among which are the temperature and aging of the screen matrix. This latter effect is especially relevant for Organic Light Emitting Diode (OLED) -based displays, which show a significant degradation of brightness performance throughout their lifetime [30].

C. Light power measurement

The alternative solution, first introduced by [16], involves the direct measurement of the outputted radiant flux density via a light power sensor. This approach enables the direct characterization of the screen radiant flux crossing the camera pupil, thus avoiding approximation errors and uncertainties associated with modeling. This section describes how the optical output of a single screen pixel can be accurately measured using a commercial light power sensor.

The measurements are acquired through a light power meter placed exactly at the location of the camera pupil. Note that, for the experiments discussed in this paper, a Thorlabs S130C photodiode sensor* has been used. When the photodiode is exposed to light, it generates an electrical current I_m that is sampled by a high-accuracy analog-to-digital converter. Since the sensor sensitivity varies with the wavelength of the incoming light, the manufacturer provides a calibrated sensitivity curve to enable the conversion of the measured current into incoming radiant flux P_m. In particular, the sensor current I_m is given by:

$$I_m = \int_0^{\infty} P_\lambda(\lambda)\, S(\lambda) d\lambda \tag{11}$$

where $P_\lambda(\lambda)$ is the spectral radiant flux impacting the sensor and $S(\lambda)$ is the sensitivity curve of the photodiode as a function of the wavelength λ, shown in Fig. 3 for reference. As can be noted, the S130C power meter is sensitive in a broad spectrum ranging from long ultraviolet (i.e., 370 nm) to near infrared (i.e., 1120 nm).

In the case of monochromatic or narrow-spectrum light sources with a given wavelength $\bar{\lambda}$, such as lasers, the radiant flux can be directly computed as:

*Thorlabs S130C product web-page: `https://www.thorlabs.com/thorproduct.cfm?partnumber=S130C`, last accessed in Jul. 2025.

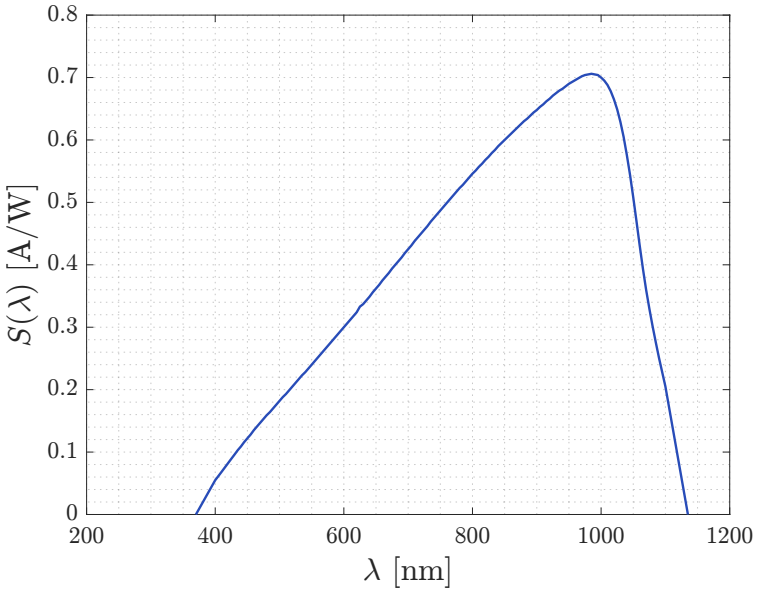

Fig. 3 Thorlabs S130C power meter sensitivity curve.

$$P_m = \frac{I_m}{S(\bar{\lambda})} \tag{12}$$

Differently, the conversion is more complex for broad-spectrum emitters as each spectral contribution is characterized by a different sensitivity value. In this case, the total power is the integral of the spectral radiant flux over the wavelength domain:

$$P_m = \int_0^\infty P_\lambda(\lambda)\, d\lambda = \int_0^\infty k_P \hat{P}_\lambda(\lambda)\, d\lambda \tag{13}$$

In the second part of Eq. (13), the unknown spectral radiant flux $P_\lambda(\lambda)$ has been decomposed into two components: a relative spectral distribution function $\hat{P}(\lambda)$ and a multiplicative constant factor k_P. The former component $\hat{P}(\lambda)$ expresses the normalized distribution of the spectrum of the emitter. This curve can be obtained from the screen manufacturer or measured using a spectrometer. For reference, the $\hat{P}(\lambda)$ curve of the screen of the TinyV3RSE facility is reported in Fig. 4. As can be noted, the display spectrum is characterized by three peaks in correspondence with the red, green, and blue OLED sub-pixel channels.

Substituting the definition of $P_\lambda(\lambda) = k_P \hat{P}_\lambda(\lambda)$ into Eq. (11), it is possible to compute the multiplicative factor k_P, which can be inserted into Eq. (13) to obtain the radiant flux P_m:

$$P_m = \int_0^\infty \frac{I_m}{\left(\int_0^\infty \hat{P}_\lambda(\lambda) S(\lambda) d\lambda\right)} \hat{P}_\lambda(\lambda) d\lambda \tag{14}$$

Note that this method is valid only in the case in which the screen spectrum is within the range of the sensor.

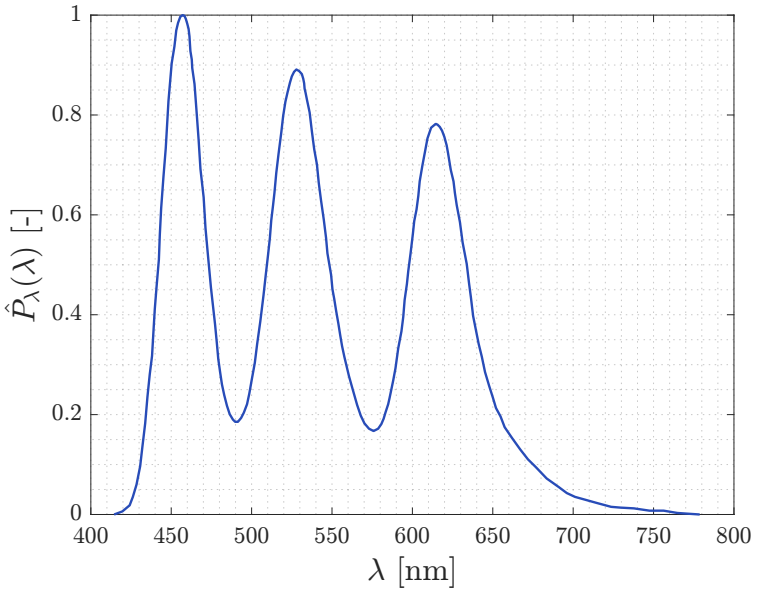

Fig. 4 Relative spectral emissivity of TinyV3RSE display.

To accurately perform the measurement using Equation (14) it is necessary to have the knowledge of the relative spectral distribution $\hat{P}_\lambda(\lambda)$. In case the $\hat{P}(\lambda)$ curve cannot be retrieved, the spectrum of the screen can be approximated as the combination of three Dirac-delta functions, one for each of the color peaks. This method is inherently suboptimal, as it limits the applicability of the more accurate spectral formulations presented earlier. The resulting calibration error depends on how well the chosen wavelengths capture the actual emission distribution peaks and on the smoothness of the light power sensor sensitivity curve. For these reasons, this approximation is more accurate when the peaks are narrow, such as in the case of LED-based screens that are generally characterized by sharp spectral emittance.

The peak wavelength of the red, green, and blue peaks (λ_r, λ_g, and λ_b, respectively) can be estimated starting from the CIE 1931 chromaticity coordinates, which are commonly accessible values in the screen datasheets. In particular, there exist several methods for converting the CIE (x, y) coordinates into dominant wavelength values. The simpler method consists of using the CIE 1931 chromaticity diagram [31, 32] to manually derive the wavelength on the horseshoe-shaped curve. Other methods, such as the one of [33], are numerical-based, allowing an accurate computation of the dominant wavelengths. When this approximation is used, the total radiant flux is computed by summing up the three-color contributions:

$$P_m = P_{m_r} + P_{m_g} + P_{m_b} = \frac{I_{m_r}}{S(\lambda_r)} + \frac{I_{m_g}}{S(\lambda_g)} + \frac{I_{m_b}}{S(\lambda_b)} \tag{15}$$

Note that each of the three current levels I_{m_r} (red), I_{m_g} (green), and I_{m_b} (blue) must be measured individually, by lighting up a single type of sub-pixels at a time.

The measurements are acquired at each digital count B to characterize the dynamic range of the stimulator. Since

the lower range of the sensor is greater than the power emitted by a single pixel, especially at low digital count levels, the measurements are made by lighting a square of N_p^2 pixels, similarly to the procedure outlined in [16]. The radiant flux density at the pupil for a single pixel on the boresight F_0 is therefore computed by taking into account the different contributions of all the pixels composing the square. In particular, the radiant power measured by the sensor decreases with a factor of $\cos^3(\varphi)\cos(\theta)$, in which the contribution of $\cos^3(\varphi)$ derives from Eq. (9) and the $\cos(\theta)$ term accounts for the projected pupil area of the sensor. Therefore, the value of F_0 can be computed as:

$$F_0 = \frac{P_m}{A_m} \frac{1}{\sum_{i=1}^{N_P^2} \cos^3(\varphi_i)\cos(\theta_i)} \tag{16}$$

where φ_i is the inclination angle of the chief ray departing from the center of each pixel composing the illuminated square portion, θ_i is the inclination of the same ray reaching the pupil, and A_m is the area of the light sensor aperture. Thanks to Eq. (16), it is possible to accurately compute the value of radiant flux density produced by a boresight pixel even when its intensity is below the sensitivity limit of the sensor. Indeed, the cosine terms summation is negligible only for small squares that span a few degrees of FoV, but becomes relevant when larger pixel squares are used.

D. Spectral equivalence between stimulator and real scenario

As shown in Fig. 4, the screen of a typical stimulator is characterized by a distinctive spectral profile that is markedly different from that of real objects. In particular, its peculiar three-peak shape is confined to the visible portion of the spectrum, whereas real objects may also have significant emissions in the infrared (IR) and ultraviolet (UV) bands. Because of the different emitting distributions, the exact spectral characteristics of real scenarios cannot be reproduced in a facility. What can be done is to ensure the camera produces an equivalent response to that of a real scenario. In other terms, the electron flux in each pixel of the camera sensor should match the one that would be measured by observing a real scenario. It is worth noting that this is not an approximation since the image digital count is the result of the integral contribution of the photons in each wavelength. In particular, the electron flux in a pixel P_{e^-} is given by:

$$P_{e^-} = \int_0^\infty Q(\lambda)T(\lambda)\frac{\lambda}{hc}P_\lambda(\lambda)d\lambda \tag{17}$$

where $Q(\lambda)$ is the quantum efficiency, defined as the ratio of produced electrons to incident photons for each wavelength λ, $T(\lambda)$ is the transmissivity of the camera lens, and P_λ is the spectral radiant flux reaching the pixel. The term $\frac{\lambda}{hc}$ expresses the inverse of the photon energy, where $h = 6.626 \cdot 10^{-34}$ J/Hz is the Planck's constant and $c = 29979258$ m/s is the speed of light in a vacuum. To compute the electron flux, it is necessary to determine the spectral radiant flux $P_\lambda(\lambda)$ acquired at each pixel. This is determined by multiplying the radiant flux density $F_\lambda(\lambda)$ in the direction of the pixel by the projected pupil area:

$$P_\lambda(\lambda) = F_\lambda(\lambda)\, A_p \cos(\theta) \tag{18}$$

It is worth noting that Equation (17) is valid both for a camera observing a real scene and for a camera stimulated inside a HIL facility, provided that the spectral radiant flux density is expressed with the associated spectral profile. From this point forward, the spectral radiant flux density of the real scene and the stimulator are denoted as $F_\lambda^{(r)}(\lambda)$ and $F_\lambda^{(h)}(\lambda, B)$, respectively. This underlines the distinction between the spectral radiant flux density of a real scene and the one to be mimicked by the stimulator. Note that the value of $F_\lambda^{(h)}$ has a direct dependence on the screen digital count B, which is the variable controlling the dimming of the pixel.

To ensure an identical pixel response, the value of P_{e^-} must be the same in both scenarios:

$$P_{e^-}^{(r)} = \int_0^\infty Q(\lambda)T(\lambda)\frac{\lambda}{hc}F_\lambda^{(r)}(\lambda)\, A_p \cos(\theta) d\lambda \triangleq \int_0^\infty Q(\lambda)T(\lambda)\frac{\lambda}{hc}F_\lambda^{(h)}(\lambda, B)\, A_p \cos(\theta) d\lambda = P_{e^-}^{(h)}(B) \tag{19}$$

where the symbol $\triangleq$ underlines that the equivalence is not a direct derivation, but a volountary enforcement of the outlined methodology. In essence, the radiometric emulation problem involves finding the digital count B for which Eq. (19) holds true.

To further simplify the equations, let the normalized quantity $\eta(\lambda)$ be defined as:

$$\eta(\lambda) = \frac{Q(\lambda)T(\lambda)\lambda}{\max_\lambda\left(Q(\lambda)T(\lambda)\lambda\right)} \tag{20}$$

Given its definition, the curve $\eta(\lambda)$ is normalized between 0 and 1 and expresses the relative response of the camera to the spectral energy flux received at each wavelength. By substituting the definition of $\eta(\lambda)$ and carrying out the needed simplifications, Eq. (19) can be written as:

$$F_{\text{eff}}^{(r)} = \int_0^\infty \eta(\lambda)F_\lambda^{(r)}(\lambda)\, d\lambda \triangleq \int_0^\infty \eta(\lambda)F_\lambda^{(h)}(\lambda, B)\, d\lambda = F_{\text{eff}}^{(h)}(B) \tag{21}$$

The quantity F_{eff}, defined from here on as "effective radiant flux density", is a non-physical quantity for comparing the effects measured by a camera generated by sources with different spectra. The left-hand side of Eq. (21) expresses the effective radiant flux density of a real scene, which shall be reproduced by the stimulation. The value of $F_{\text{eff}}^{(r)}$ has to be computed during the rendering process for each element composing the discretized grid of angular direction displayed on the screen. Differently, the right-hand side is the value of $F_{\text{eff}}^{(h)}(B)$ that the facility can produce, which is characterizable as a function of the digital count B through the power meter measurements. In particular, the $F_{\text{eff}}^{(h)}(B)$ curve is computable assuming a spectral radiant flux density expressed as:

$$F_{\lambda}^{(h)}(\lambda, B) = F_0(B)\ \cos^3(\varphi)\ \frac{\hat{P}_{\lambda}(\lambda)}{\int_0^{\infty} \hat{P}_{\lambda}(\lambda) d\lambda} \tag{22}$$

Where $F_0(B)$ is the radiant flux density produced by a pixel on the boresight (Eq. (16)) and the cubic cosine term accounts for the observational geometry. The actual dependency on λ is expressed by the profile $\hat{P}_{\lambda}(\lambda)/\int_0^{\infty} \hat{P}_{\lambda}(\lambda) d\lambda$, which is defined to have a unitary integral since $\hat{P}_{\lambda}$ is normalized between 0 and 1 at its maximum value.

Note that the $F_{\text{eff}}^{(h)}(B)$ curve is not only influenced by the spectral properties of the stimulator components, but also by the radiometric response of the camera, which is expressed by the η curve. Because of this, a specific calibration curve is valid for a single combination of camera, screen, and geometry. As shown by [19], in the case of variable-magnification facilities, the magnification value affects the radiometric calibration curve, with high-magnification setups being significantly brighter than the ones configured to stimulate cameras with larger FoVs.

E. Scene generation

The goal of the rendering process is to compute the value of the effective radiant flux density $F_{\text{eff}}^{(r)}$ that should be reproduced by each screen pixel. In this context, the array of screen pixels represents a grid of angular directions, in which each pixel projects light in a specific direction perceived by the observing camera.

On one hand, the effective radiant flux density is independent of the geometrical properties of the camera (e.g., pupil size), making it a suitable metric for characterizing the optical output of the stimulator itself. On the other hand, because it results from the integration of spectral quantities, its accurate computation requires careful consideration of the spectral characteristics of the scene being emulated. Once the value of $F_{\text{eff}}^{(r)}$ for each pixel is computed, it can be converted into an equivalent value of screen digital count B using the previously determined radiometric calibration curve $F_{\text{eff}}^{(h)}(B)$.

The computation of the $F_{\text{eff}}^{(r)}$ matrix can follow different logics depending on the type of objects within the images, with a fundamental distinction between resolved and unresolved sources. A common operational criterion defines unresolved objects as those whose apparent angular size is smaller than one camera pixel. However, more meaningful criteria relate to the observability of object features. In this sense, an object should be considered resolved when its structural or radiometric characteristics -such as shape or variations in surface emission- can be distinguished in the acquired image. The angular size threshold after which an object can be considered resolved depends on several factors, including the object's shape complexity and the exposure conditions. The camera's Point Spread Function (PSF) plays a central role, as its blurring effect can significantly mask features when high illumination conditions are met. In general, this second definition will be assumed throughout the rest of this paper.

1. Unresolved objects

In the case of unresolved objects, the computation of $F_{\text{eff}}^{(r)}$ is simplified. In this case, all of the radiant flux can be reasonably assumed to originate from a single direction; therefore, a single screen pixel is sufficient to reproduce the object.

The computation of the value of $F_{\text{eff}}^{(r)}$ through the left-hand side of Eq. (21) requires the knowledge of the spectral response $F_{\lambda}^{(r)}(\lambda)$ of the object. This curve can be expressed as the multiplication of a constant factor k_s and a relative spectral profile $\hat{F}_{\lambda}^{(r)}(\lambda)$, which is normalized between 0 and 1:

$$F_{\lambda}^{(r)} = k_s \, \hat{F}_{\lambda}^{(r)}(\lambda) \tag{23}$$

Computing the value of k_s requires information about the actual brightness of the object, which is usually expressed by the magnitude. In particular, the magnitude expresses the ratio between the irradiance F_X in a given band X and the reference irradiance for that filter band $F_X^{(0)}$, also known as filter zeropoint:

$$m_X = -2.5 \log_{10} \left(\frac{F_X}{F_X^{(0)}} \right) \tag{24}$$

Moreover, F_X is given by:

$$F_X = \int_0^{\infty} F_{\lambda}^{(r)}(\lambda) X(\lambda) d\lambda \tag{25}$$

where $X(\lambda)$ expresses the relative transmissivity of a generic photometric filter [34]. This curve is tabulated for each filter and normalized to have a peak value of 1. At this point, the value of the constant factor k_s can be computed by combining Eq. (25) and Eq. (23) and solving for k_s:

$$k_s = \frac{F_X}{\int_0^{\infty} \hat{F}_{\lambda}^{(r)}(\lambda) \; X(\lambda) d\lambda} \tag{26}$$

By starting from these preliminary considerations, it is important to discriminate between stars and other celestial objects. This is mainly because their radiometric emulation in the stimulator requires different radiometric modeling.

Stellar objects can be geometrically reproduced thanks to the information provided by stellar catalogs, such as Hipparcos [35] and Tycho [36], where the right ascension and declination are reported with sub-arcsecond accuracy. Two quantities must be retrieved from the catalogs to emulate star radiometry: the radiometric magnitude and the color index. The magnitude - often expressed for the visual band V - is used to compute the radiant flux density F_V inverting Eq. (24). Conversely, the color index expresses the difference in magnitude between two radiometric bands and can be used to estimate the spectral profile of the incoming light. In practice, stellar objects are often approximated as black

bodies, having a normalized spectral profile of the form:

$$\hat{F}_{\lambda}^{(r)}(\lambda) = \frac{M_{BB}(\lambda)}{\max_{\lambda}(M_{BB}(\lambda))} \tag{27}$$

where the black body spectral exitance $M_{BB}(\lambda)$ is given by Planck's law:

$$M_{BB}(\lambda) = \frac{2\pi hc^2}{\lambda^5} \frac{1}{\exp\left(\frac{hc}{\lambda K_B T_{\text{eff}}}\right) - 1} \tag{28}$$

with $K_B = 1.381 \cdot 10^{-23}$ J/K being the Boltzmann constant. Planck's law has a dependence upon the object effective temperature T_{eff}, which can be approximated for a star from the color index. For example, the empirical formula provided by [37] is based upon the (B-V) color index, which is the difference between the blue (B) and visual (V) magnitudes:

$$T_{\text{eff}} \approx 4600 \left(\frac{1}{0.92\ (B\text{-}V) + 1.7} + \frac{1}{0.92\ (B\text{-}V) + 0.62}\right)\ [\text{K}] \tag{29}$$

This approximation is considered fairly accurate for main-sequence stars, although there exist more refined models that take into account other parameters such as the metallicity and the color index between additional bands [38].

The reproduction of unresolved planets and asteroids is more complex as they are characterized by spectra with variable emissions and intensities. Indeed, their apparent magnitude is strongly influenced by the observational geometry and by the absorption spectrum of their surfaces and/or atmospheres. Empirical models are available to express their magnitude as a function of the current phase angle and distances between the Sun, the object, and the observer [39]. These models are often expressed in the form proposed by Müller [40], involving polynomials as a function of the observational phase angle α:

$$m_V = 5 \log_{10}(rd) + m_V^{1\text{AU}} + C_1\alpha + C_2\alpha^2 + \ldots \tag{30}$$

where r and d are the distances in AU between the observer and the planet and between the planet and the Sun, respectively. $m_V^{1\text{AU}}$ expresses the planet's absolute magnitude: the magnitude perceived at $\alpha = 0$, placing the celestial body at 1 AU from both the Sun and the observer. There also exist more detailed formulations accounting for the impact of additional contributions, such as Mars seasonal changes and Saturn rings [39].

The spectral profile of each planet can be retrieved from advanced tools such as NASA's Planetary Spectrum Generator (PSP) [41]. This tool computes the spectral emission profile of each planet, accounting for atmospheric opacity, scattering, and surface absorption. Using the PSP it is possible to directly retrieve the normalized spectral irradiance profile $\hat{F}_{\lambda}^{(r)}(\lambda)$, which can be used in combination with the magnitude information to compute the scaling factor k_s in Eq. (26).

Note that, for reasons dictated by the geometric calibration, when reproducing an unresolved object, it may be useful to split the total contribution of $F_{\text{eff}}^{(r)}$ computed so far into multiple pixels. This is done to reproduce the line-of-sight direction of the object with sub-pixel accuracy, overcoming the limit posed by the use of a single pixel. The results shown in this work have been obtained leveraging the technique described in [21].

2. Resolved objects

When the scenes involve resolved objects, the light that they emit is distributed into multiple pixels. The optical emulation in a HIL facility requires the computation of the radiometric intensity that shall be reproduced by each pixel. To do so, advanced rendering tools are required to obtain optimal radiometric and geometric accuracy. Several of these tools, most notably SurRender and PANGU, have been developed by space actors to support the development of vision-based navigation techniques.

SurRender [42], developed by Airbus Defence & Space, is a proprietary rendering tool tailored for space operations. It is capable of physical-based rendering via ray tracing techniques. PANGU [43] (Planet and Asteroid Natural Scene Generation Utility) has been developed by the University of Dundee with ESA support. It provides a high-fidelity toolset designed for generating optical, thermal, and LiDAR images of planetary bodies.

Both tools have restricted access, being either proprietary or closed-source. This fact has brought the community to seek open-source alternatives. Among these, an example is CORTO [44], which is based on the Blender rendering software. Despite Blender not providing spectral and physical consistency in the image rendering process, recent work [45] has developed a calibration procedure to align Blender RGB output with the required values of radiant flux densities. This calibration tool has been expanded into a stand-alone physical-based render engine named ABRAM [46], able to produce geometrically and radiometrically validated images for quasi-spherical celestial objects, such as planets and moons. Note that all the resolved scenes in this paper have been rendered with ABRAM, unless otherwise specified. An example of the rendered $F_{\text{eff}}^{(r)}$ map for a Moon navigation scenario is shown in Fig. 5.

III. Hardware validation

A. Stimulators setup

The proposed radiometric calibration and emulation methodology has been applied and tested in both optical stimulators assembled by the DART Lab: TinyV3RSE and RETINA. As these are characterized by different designs, the use of two different stimulators allows more comprehensive tests of the proposed procedure, showing its applicability to a wide range of setups. For the sake of completeness, the main characteristics of the TinyV3RSE and RETINA facilities are reported in Table 1.

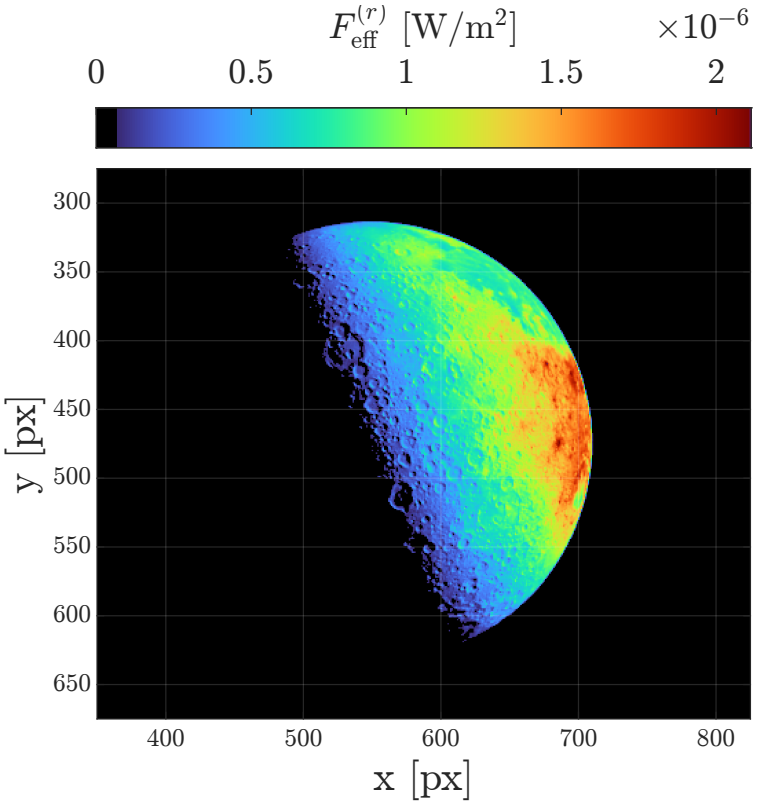

Fig. 5 Example of Moon $F_{\text{eff}}^{(r)}$ map rendered via ABRAM for TinyV3RSE.

Table 1 Characteristics of the optical stimulators.

Facility	TinyV3RSE [20]	RETINA [21]
Magnification type	Fixed	Variable
Display	Galaxy-S7	WUXGA-R5
Resolution	2560 x 1440	1920 x 1200
Refresh rate	0.3 Hz	85 Hz
Max. diagonal FoV	28°	4°-22°
Max. pupil diam.	36 mm	15 mm

For the following tests, a FLIR BFS-U3-31S4[†] industrial-grade camera was installed in RETINA. The camera is equipped with a 25 mm objective. Consequently, the distance between the collimator and relay lens systems has been adjusted to achieve a magnification level that ensures the matching between the camera FoV and the screen size. The tests performed TinyV3RSE are executed with a high-TRL Leonardo AA-STR MKII[‡] star tracker [47]. The device is the latest evolution of a medium-FoV star tracker family with a large flight heritage of both commercial and space exploration missions. The star tracker is used in the context of the ESA-funded STAR Nav project [48], which investigates the feasibility of its use as an optical navigation sensor leveraging optical navigation algorithms [49, 50].

[†]FLIR BFS-U3-31S4 spec-sheet: `http://softwareservices.flir.com/BFS-U3-31S4/latest/Model/spec.html`, last accessed in Jul. 2025.

[‡]Leonardo AA-STR product web-page: `https://electronics.leonardo.com/en/products/aastr`, last accessed in Jul. 2025.

One of the outputs of the STAR Nav project is a publicly available dataset of Moon images acquired by the star tracker using the radiometric calibration framework described in this paper [51].

Table 2 Characteristics of the employed optical devices.

Device	FLIR BFS-U3-31S4	AA-STR MK2.0
Facility	RETINA	TinyV3RSE
Resolution	2048 x 1536	1024 x 1024
Sensor type	CMOS	CMOS
Pixel pitch	3.45 µm	18 µm
Focal length	25.0 mm	50.7 mm
FoV	16.1° x 12.1°	20.6° x 20.6°
Exposure time	10 µs - 30 s	200 ms* - 6 s

* Full frame acquisition. 20 ms when acquiring small windows.

The characteristics of the two optical devices are summarized in Table 2. As can be noted, the AA-STR star tracker has a more restricted exposure time range compared to the industrial camera. This limitation stems from its hardware, which is specifically designed for the continuous acquisition and tracking of small windows containing individual stars. In particular, its minimum exposure time is limited at a fairly high value of 200 ms, causing evident blooming and over-saturation effects when imaging bright resolved objects [48]. As shown in Section III.D, these effects significantly impact the acquired images and consequently the geometrical accuracy of the image processing outputs.

Figure 6 shows the relative energetic efficiency curve $\eta(\lambda)$ of the two optical devices. It is worth underlining that the curve of the FLIR BFS-U3-31S4 camera is computed assuming a constant lens transmissivity throughout the entire spectrum since no data about the radiometric properties of the lens could be retrieved or obtained by the manufacturer.

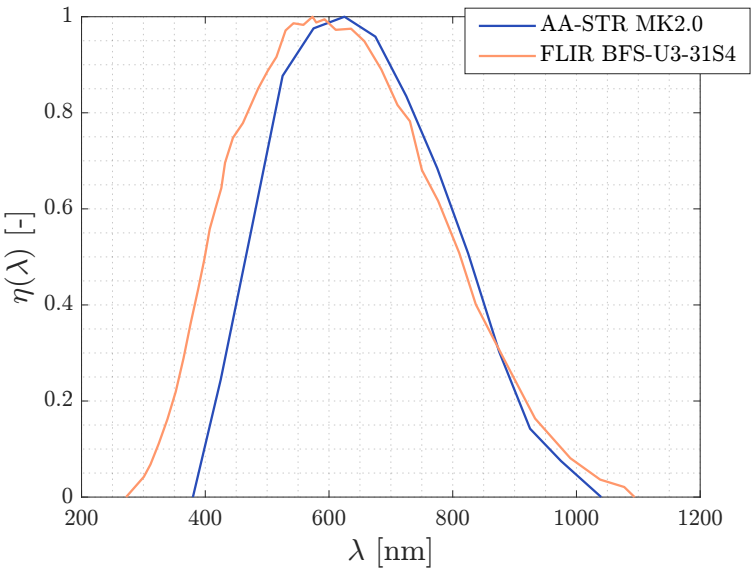

Fig. 6 Relative energetic efficiency curve of optical devices.

This assumption is not expected to impact the accuracy of the radiometric calibration since optical glasses are in any case usually characterized by an almost constant transmissivity in particularly in the visual range [52].

B. Stimulator calibration

Starting from the data in Fig. 6 and the measurements from the light power meter, it is possible to compute the calibration curves of the two stimulators, as reported in Fig. 7. Note that the digital count units $[DC_8]$ in the figure are expressed in an 8-bit range, hence the subscript. The curves were computed using the procedure detailed in Sections II.C and II.D.

For TinyV3RSE, the power meter radiant flux P_m has been computed as described in Eq. (14), leveraging the knowledge of the relative spectral emission curve of the screen already shown in Fig. 4. For RETINA, this information could not be retrieved. For this reason, the P_m value has been computed accounting for the separate contributions of each color channel, as shown in Eq. (15). In this case, the three color wavelengths $\lambda_r = 635$ nm, $\lambda_g = 544$ nm, and $\lambda_b = 475$ nm have been estimated through the inversion of the CIE 1931 chromaticity diagram using the CIE (x, y) coordinates stated by the display manufacturer.

Comparing the two curves, it can be noted how the TinyV3RSE setup provides a maximum effective radiant flux density value (i.e., for $B = 255$) that is 25 % greater than the one of RETINA. As a result of this, brighter objects can be emulated in the former testbed. On the other hand, the setup of RETINA seems to retain better linearity and control, especially at low digital count levels. This results in a higher overall dynamic range ($2.4 \cdot 10^4$ for RETINA and $1.7 \cdot 10^4$ for TinyV3RSE), which is a useful feature when reproducing objects spanning several orders of magnitude. Overall, the radiometric calibration curves do not show a linear evolution over the whole screen dynamical range, resulting in

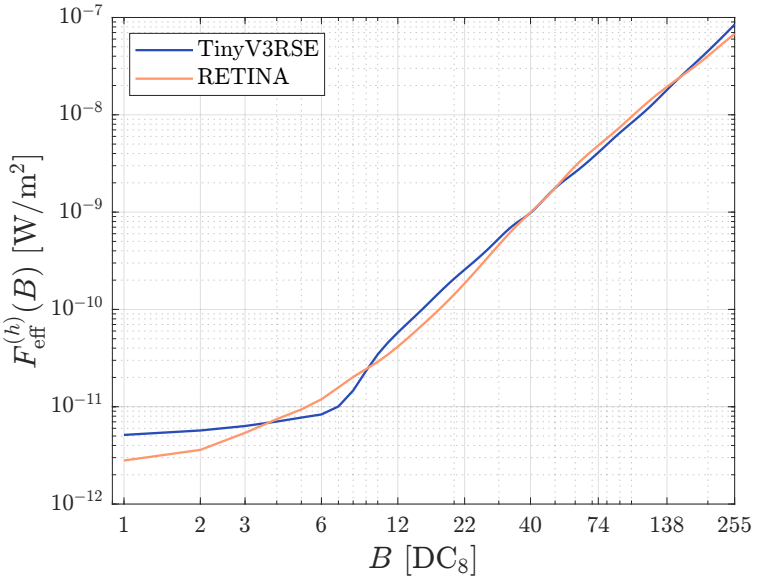

Fig. 7 Radiometric calibration curve of the two stimulators.

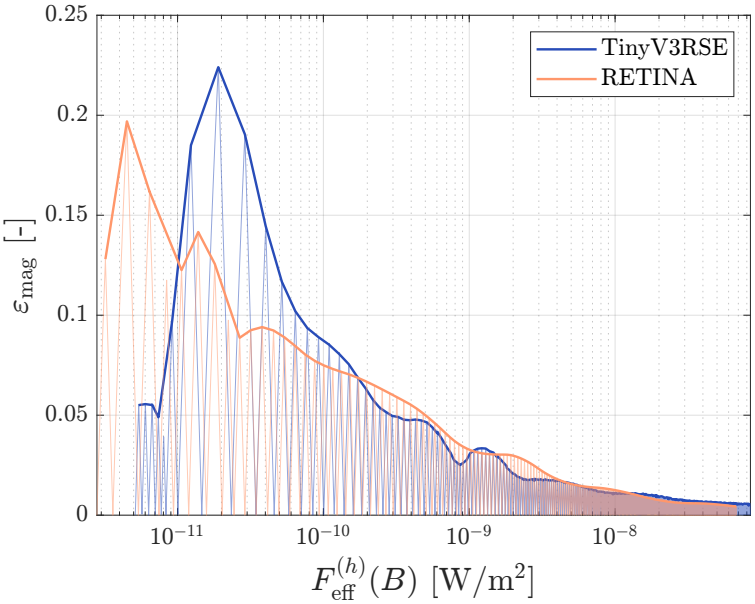

Fig. 8 Relative quantization magnitude error for the two stimulators. Bold lines identify envelope of maximums.

the need for an accurate radiometric characterization of the optical stimulator before its use. This confirms previous experiments reported in [19] and analyses shown in [17].

It is important to note that an inevitable quantization error is committed due to the discretized nature of the digital count, when the $F_{\text{eff}}^{(h)}(B)$ is inverted to compute the necessary digital count value B. The relative error committed at each radiant flux density value and its maximum value envelope are shown in Fig. 8 for the two stimulators. The error ε_{mag} is expressed in terms of magnitudes, computed via Eq. (24).

As expected, the relative error is higher at low digital count levels due to the exponential nature of the screen responses. The relative error can reach up to 0.22 magnitudes (circa 23 %) of the reproduced value. However, for higher radiant flux values, the quantization error is systematically below 0.05 magnitudes.

C. Intensity scaling

Unfortunately for most space applications, the $F_{\text{eff}}^{(r)}$ values are systematically larger than the maximum value reproducible by the screen [48, 53]. By performing an analysis of the screens available on the market, there exists no screen capable of delivering the level of radiant flux required for simulating close- and medium-range scenarios around celestial bodies. For example, the maximum output of TinyV3RSE ($F_{\text{eff}}^{(h)}(B = 255) = 8.47 \cdot 10^{-8}$ W/m^2) is evidently below the values required to simulate the Moon in the scenario of Fig. 5. In this case, the stimulator appears to be about 25 times less luminous than required. Similar considerations have been identified for other applicative scenarios at the Jovian moons, as reported in [53].

For these reasons, a scaling methodology has been engineered to overcome the limitations of the optical testbed and

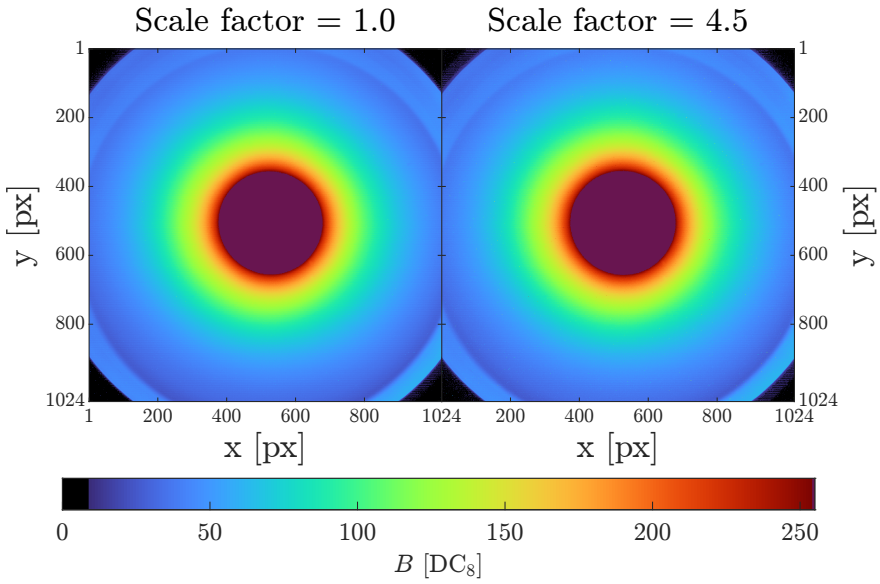

Fig. 9 Comparison between images obtained scaling the exposure time and radiometric output.

allow performing HIL tests leveraging the accurate calibration procedure described so far. Given that the exposure time and the received radiant power both linearly contribute to determining the radiant energy and therefore the pixel response, they can be reasonably scaled to achieve the same energy. In this case, the scaling consists of increasing the exposure time of the camera to compensate for the limited brightness of the screen.

A comparison test is performed to validate the proposed scaling. During the test, a disk with a radius of 150 pixels is displayed on the screen. Each disk pixel is illuminated with a nominal $F_{\text{eff}}^{(r)}$ value equal to the maximum value reproducible by TinyV3RSE. The nominal exposure time is set to 200 ms, which is the minimum allowable by the star tracker hardware. In subsequent images, the disk brightness is reduced and the exposure time is increased, ensuring the equivalence among the radiant energies.

Figure 9 shows a comparison between two images: one captured under nominal conditions, and another acquired using a scale factor of 4.5, corresponding to an exposure time of 900 ms. Due to the high illumination levels used in this test, the image is significantly saturated and exhibits noticeable blooming. This phenomenon arises from the leakage of electron charges from saturated pixels into adjacent ones [54, 55]. The stochastic nature of this effect makes it difficult to predict accurately and highly nonlinear. Nevertheless, aside from an increased noise level in the scaled image, both images appear visually equivalent, indicating consistent radiometric emulation across exposure conditions.

The same test is repeated for several scaling factor levels. The resulting Cumulative Distribution Function (CDF) and Probability Distribution Function (PDF) of the acquired images for the tested cases are shown in the top portion of Fig 10. As can be seen, all the images are characterized by peculiarly similar pixel intensity distributions. The lower portion of Fig 10 highlights the differences (Δ CDF) between the CDF of the images at each scaling factor and the CDF of the one obtained with the native exposure time. As the plot shows, the maximum difference in cumulative probability

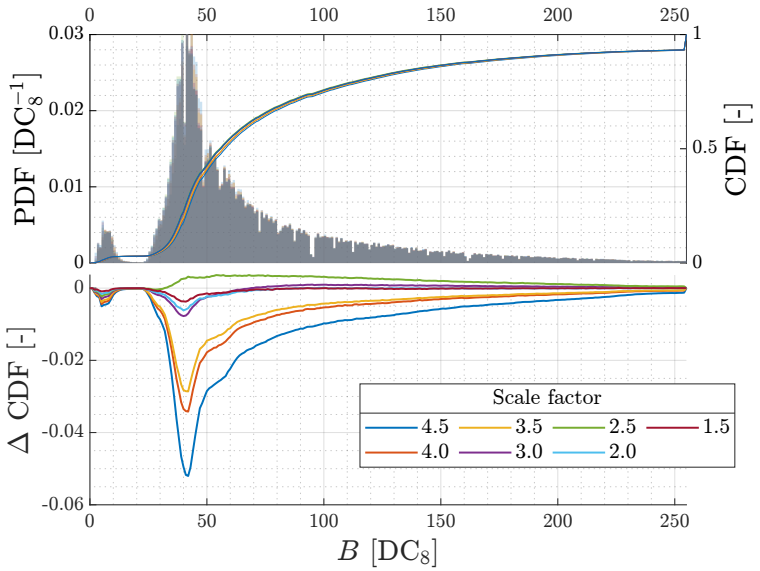

Fig. 10 CDF and PDF comparison between different scaling factors.

distribution is solidly less than 0.06. The results of this test hint not only at the validity of the scaling framework but also at the overall consistency of the radiometric calibration on a relative level.

As mentioned, increasing the exposure time inevitably introduces additional noise into the acquired images, representing a limitation of this strategy. In this framework, such conditions are interpreted as a worst case: algorithms that remain robust under these higher-noise scenarios are expected to perform even better under normal conditions. The actual impact of added noise on the performance of those algorithms depends on their sensitivity to signal-to-noise ratio variations. If necessary, controlled denoising or corrective image-processing techniques may be applied to mitigate the impact while retaining the overall radiometric fidelity.

D. End-to-end validation tests

Starting from the developed radiometrical calibration and the intensity scaling, an end-to-end validation of the radiometric emulation methodology is performed. The main idea behind this test is to generate images with a radiometric-validated renderer and to compare them with the ones acquired in the facility. The comparison between the two ensures that the radiometric calibration is well performed, guaranteeing the correct level of electron flux measured by the detector.

The end-to-end test is performed as follows. First, a homogeneous sphere with a Lambertian bidirectional reflectance distribution function (BRDF) is rendered through the ABRAM tool. Two scenes are computed: one considering opto-geometrical characteristics of the AA-STR star tracker and another to be displayed in TinyV3RSE, appropriately converted through the calibration curve. Given that the spectral characteristics of the star tracker can be modeled in ABRAM, the former image is used as a ground truth for comparison against the image acquired in the facility. It is

worth noting that ABRAM has been validated against mission images [46], implying that its output is consistent with the one expected in orbit. Therefore, the image acquired by the star tracker can be directly compared with the rendered image to verify their equivalence.

The visual comparison between the two images of Lambertian spheres with increasing intensities is shown in Fig. 11. Figure 12 shows a direct comparison of the digital count levels sampled across a horizontal stripe 100 pixels wide starting from the center of the image. As can be noted in both plots, the image emulated in the facility follows accurately the output predicted by the rendering pipeline. It is worth noting that in these images only the dimmer portion of the calibration curve is investigated. This is due to the stringent exposure time limit of the star tracker (200 ms), which leads to saturated images for screen digital count levels beyond 22. The large quantization steps characterizing the calibration curve in this region are clearly visible in the plots, appearing as separate disks of constant intensity.

To investigate brighter intensity levels, the window mode of the star tracker is used. This mode allows a minimum exposure time of 20 ms although limited to an acquisition of a 20x20 pixels region square [48]. The average intensity within the window at the center of the image is computed for several steps of sphere intensity. The resulting average digital count intensity is compared with the value expected from the rendered images, as shown in Fig. 13. As the data in the figure shows, the saturation limit is shifted at a screen digital count level close to 50 when the star tracker operates in this acquisition mode.

These results show limited digital count error between the expected stimulation output and the ground truth,

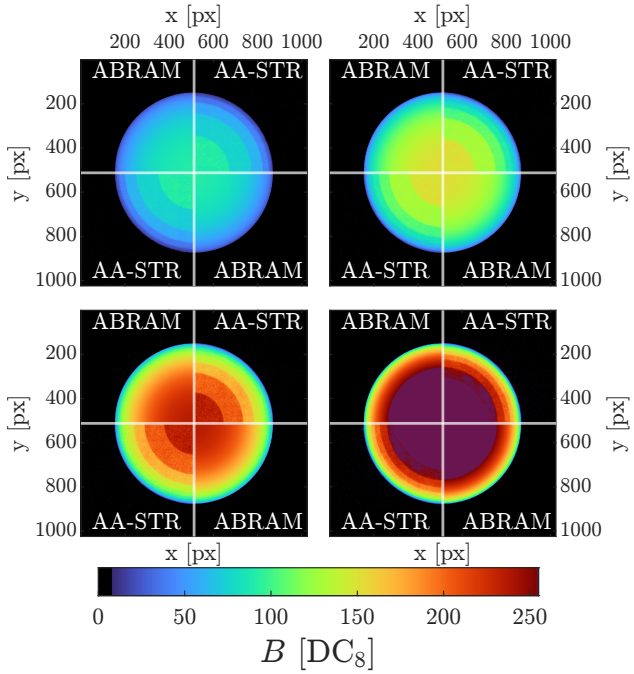

Fig. 11 Images comparison between rendered and facility-acquired Lambertian spheres with different peak intensities.

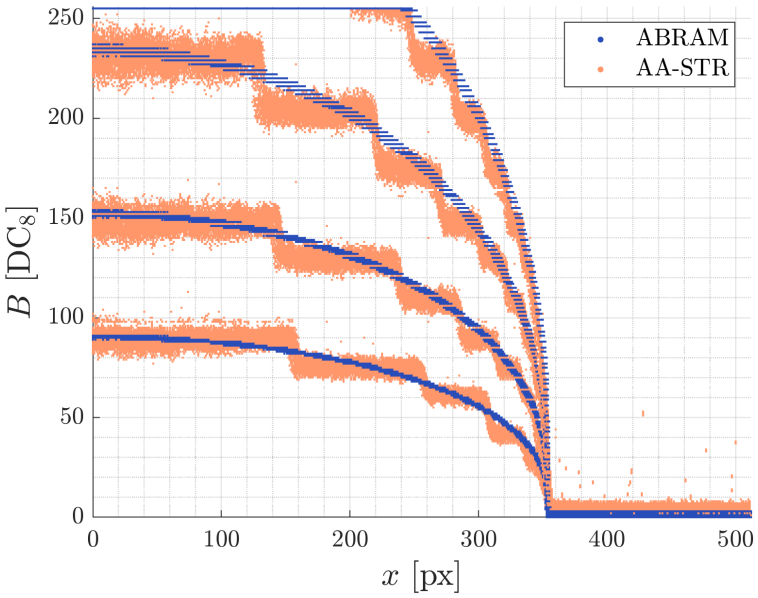

Fig. 12 Predicted and acquired digital count levels along a 100-pixel-wide stripe starting from the center of the spheres.

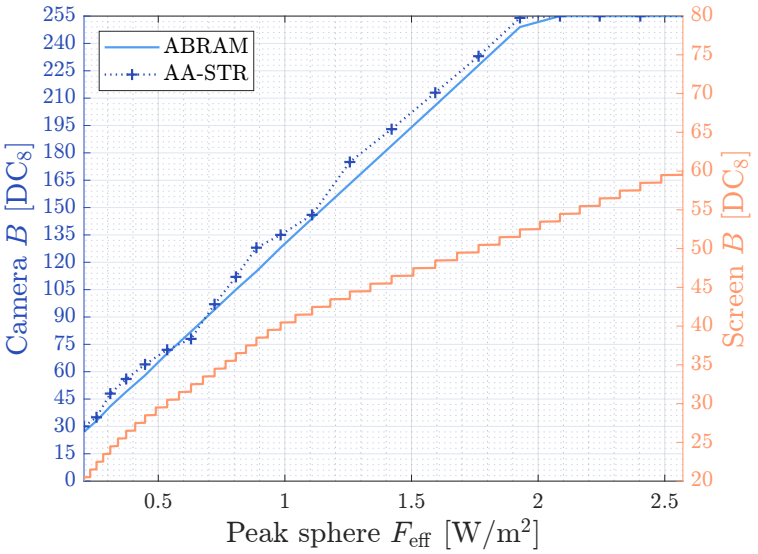

Fig. 13 Acquired and predicted camera digital count, consequent screen digital count for different peak sphere intensities.

supporting the overall consistency of the radiometric calibration both on a relative and absolute level. Indeed, it has been possible to reproduce several levels of radiant flux density on a linear scale thanks to the nonlinear mapping provided by the calibration curve.

E. Comparison with night-sky images

The results expounded so far have only investigated comparison against rendered images, leveraging the assumption of correct radiometric modeling of the scene rendered on the display. To overcome this limitation and to globally validate the radiometric calibration, the images generated within the stimulator are compared with real night-sky acquisitions of both resolved and unresolved objects. These are obtained using the same exposure time, gain, and aperture used in the stimulator to ensure a trustworthy comparison.

Figure 14 shows the comparison between two AA-STR MKII star tracker images of the Moon. The one on the right is a real night-sky image acquired with the minimum exposure time of 200 ms. The one on the left has been reproduced in TinyV3RSE, using an exposure time scaling factor of 26. The latter is consequently characterized by increased noise floor levels, as may be noticed in the left image. In this scenario, the Moon has a geometrical dimension of about 20 pixels and a phase angle of about 90 deg. Strong blooming and ghosting effects coupled with non-axial aberrations and distortions are the cause of a significant expansion of the casted silhouette. This determines the impossibility of distinguishing the limb of the Moon and any kind of geometric features.

The images have been quantitatively compared using the well-known Structural Similarity Index Measure (SSIM) method [56]. The computed similarity indexes are: 0.971 for luminance, 0.935 for contrast, and 0.940 for structure.

The limited imaging capabilities of the AA-STR MKII star tracker allow only a partial validation of the emulative capabilities of the HIL stimulators. For this reason, additional night-sky tests have been performed with the aforementioned industrial camera and compared with acquisitions performed in RETINA. Examples of these tests, involving both resolved and unresolved objects, are shown in Fig. 15 and Fig. 16.

In particular, Fig. 15 compares the same portions of images containing unresolved objects. The image emulated in RETINA has been produced through the procedure discussed in Section II.E, accounting for the spectral properties of

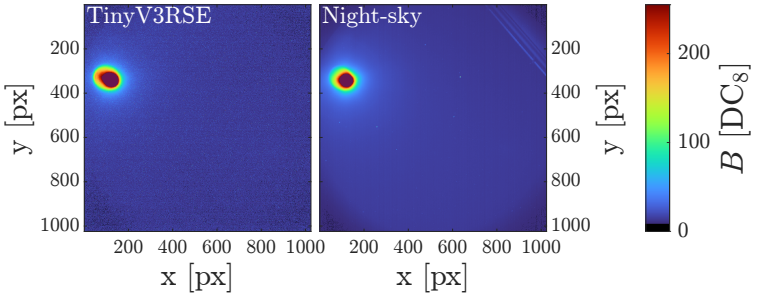

Fig. 14 Comparison between Moon images acquired with the AA-STR MKII.

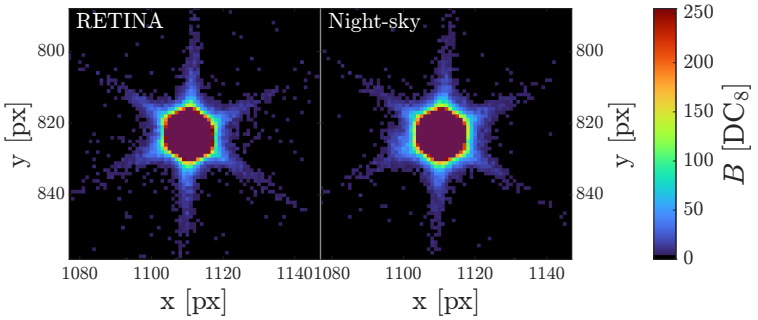

(a) Jupiter

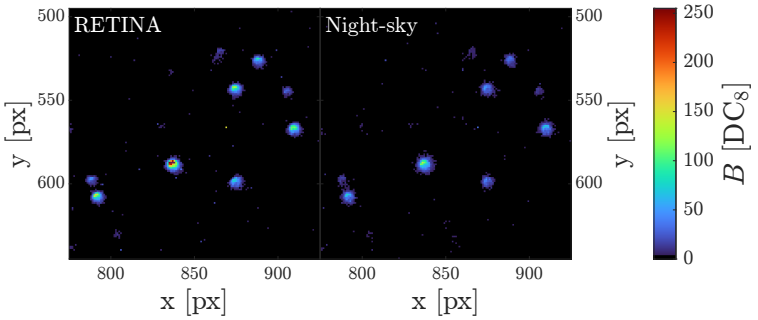

(b) Pleiades stellar group

Fig. 15 Comparison between night-sky and RETINA images for different unresolved objects.

both planets and stellar objects. On a geometrical basis, the ground truth conditions for generating the facility images are determined using ephemeris models from NASA SPICE kernels [57]. The inertial attitude of the camera is computed using classic star-centroiding techniques on the same image used in the comparison. Since no exposure time scaling is used, the illumination conditions are emulated natively in this case. The exposure time is set to 100 ms, with a digital gain of 30 dB and an aperture f-number of 4.

As can be seen, unresolved objects spanning different magnitudes can be reproduced with both geometric and radiometric accuracy. In particular, the acquisition of Jupiter (see Fig. 15a) gives rise to evident diffraction spike effects due to its brightness, as it is imaged with a visual magnitude of -2.2. These effects are cast with a hexagonal shape and are generated by the aperture-stop diaphragm of the camera objective. It is important to note that these kinds of diffraction spikes have a highly directional behavior and are strongly dependent on the opto-mechanical alignment between the internal components of the objective. For this reason, they are inherently difficult to reproduce in a rendering software, unless the complete optical design is modeled in high fidelity. This can only be done through advanced optical design tools such as Ansys OpticStudio [58] but requires the knowledge of the exact lens design and materials, which are generally not disclosed by manufacturers. In this case, thanks to the radiometric equivalence implemented in the HIL framework, it is possible to reproduce not only the shape but also the angular orientation of the diffraction effects

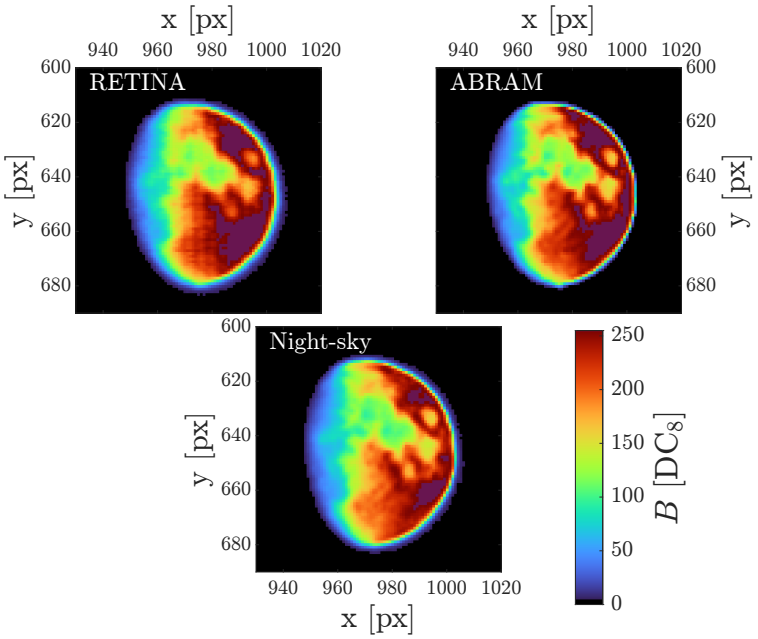

Fig. 16 Comparison between rendered images and camera images acquired in RETINA and night-sky conditions.

without prior knowledge of the opto-mechanical characteristics of the employed hardware.

The group of the Pleiades (see Fig. 15b), comprising stars with visual magnitudes above 2.84, does not saturate the detector, allowing a more detailed analysis of the geometrical accuracy of the reproduced scene. In particular, the extracted LoS directions of the star centroids in the scene are all within 9 arcsec of their respective predicted LoS. In the night-sky image, the centroids are on average 16% dimmer than their HIL counterparts. This discrepancy is expected since the simulated RETINA images do not account for atmospheric extinction effects and light pollution affecting the real image. The value of atmospheric absorption is difficult to predict since it depends on several geometrical and environmental factors, such as elevation angle, humidity, and carbonic pollution [59].

Figure 16 shows a triple comparison between a real night-sky photo of the Moon, a rendering using ABRAM, and the same emulated scene in RETINA. The stimulator image is obtained with an exposure time scaling of 15. The exposure time is set to 80 µs, with a digital gain of 15 dB and a f-number of 4. Although with this 25 mm objective setup the Moon has a size of just 60 pixels, some geometrical features are still distinguishable. Notably, some portions of the real image are affected by saturation. As expected, the real image is attenuated with respect to the emulated and rendered ones due to atmospheric extinction effects. The average transmittance factor, computed on unsaturated pixels, is 85%. This value is coherent with the expected range in clear conditions. The SSIM similarity indexes between the images are tabulated in Table 3. As can be observed, the indices show consistent levels of similarity for luminance, contrast, and structure.

In this test, an important feature that has been reproduced by the HIL setup is the moon limb expansion, which was not modeled in the ABRAM rendering. Indeed, the camera images show a considerable band of slightly lit pixels

Table 3 SSIM similarity indexes comparison.

SSIM comparison	Luminance	Contrast	Structure
RETINA - ABRAM	0.9904	0.9676	0.9389
RETINA - Night-Sky	0.9666	0.9473	0.9210
ABRAM - Night-Sky	0.9797	0.9676	0.9498

beyond the sharp limb. This effect is caused by both blooming and diffraction, with the latter having a prominent effect as shown in Fig. 15a.

IV. Conclusion

This work presents a methodology for accurately calibrating the radiometric output of optical stimulation facilities. Such calibration framework is especially relevant when conducting Hardware-In-the-Loop tests and camera stimulation experiments emulating realistic space scenes. Radiometric fidelity is a crucial aspect in those validation activities involving image processing algorithms due to the significant impact of radiometry on the overall image aspect. In such hardware-in-the-loop experiments, the lack of adequate scene fidelity can distort algorithm performance metrics and compromise the credibility of experimental results.

The proposed methodology enables the generation of radiometrically accurate scenes containing both resolved and unresolved objects. The technique is based upon external independent measurements and therefore requires limited knowledge of the hardware characteristics of the employed cameras. The developed methodology uses a light power sensor to accurately estimate the radiometric output of the optical stimulator. The measurement procedure is shown and applied to two different optical setups. This circumvents the practical limitations and inaccuracies associated with purely model-based calibration, which would otherwise require extensive, often unavailable, manufacturer-specific data.

The framework introduces the concept of effective radiant flux density as a central variable linking the output of the rendering engine to the facility's radiometric calibration. Rendering is therefore treated as the computation of a matrix in which each pixel represents the desired effective radiant flux density to be emitted by the screen. Spectral-level computations for unresolved sources, such as stars and resolved planetary bodies, are addressed in detail, enabling accurate representation across a range of scene types.

The methodology is experimentally validated on two distinct optical testbeds: one incorporating a high-TRL star tracker, and the other using a commercial industrial camera. To extend the dynamic range of the system and enable the emulation of high-brightness scenarios (e.g., lunar proximity operations), a radiometric scaling factor is introduced, and its use is validated through hardware tests. The fidelity of the overall emulation process is assessed through comparisons with both the rendered targets and real night-sky imagery. Both qualitative and quantitative results demonstrate strong consistency between the emulated and expected outputs.

The comparisons reported in this paper show that the hardware-in-the-loop framework guarantees a high level of

image fidelity, capturing hardware-related effects natively. This is especially relevant for those complex effects, such as saturation, blooming, and diffraction, that are difficult to model and predict in rendering pipelines. Thanks to the emulation procedure developed, it has been possible to investigate post-saturation blooming affecting star tracker images.

Acknowledgments

Part of the work in this paper has been conducted within the STAR Nav project (ESA Contract No. \4000139932/22/NL/CRS) within the General Support Technology Programme (GSTP) through the support of the national delegation of Italy (ASI). P.P., F.O., and F.T. are sponsored by EXTREMA, a project that has received funding from the European Research Council (ERC) under the European Union's Horizon 2020 research and innovation programme (Grant Agreement No.\864697). The authors would like to acknowledge the other members of the STAR Nav team: C. Balossi, S. Becucci, M. Belcari, L. Cappabianca, D. Macchi, F. Piccolo, and A. Sica.

References

[1] Vasile, M., Romano, M., and Trainiti, F., "An Optical Based Strategy for Deep Space Autonomous Navigation," *Spacecraft Guidance, Navigation and Control Systems, Proceedings of the 4th ESA International Conference*, Vol. 425, 2000, p. 549.

[2] Karimi, R. R., and Mortari, D., "Interplanetary autonomous navigation using visible planets," *Journal of Guidance, Control, and Dynamics*, Vol. 38, No. 6, 2015, pp. 1151–1156. https://doi.org/10.2514/1.G000575.

[3] Andreis, E., Panicucci, P., and Topputo, F., "Autonomous Vision-Based Algorithm for Interplanetary Navigation," *Journal of Guidance, Control, and Dynamics*, 2024, pp. 1–16. https://doi.org/10.2514/1.G007926.

[4] Christian, J. A., "Optical Navigation Using Planet's Centroid and Apparent Diameter in Image," *Journal of Guidance, Control, and Dynamics*, Vol. 38, No. 2, 2015, pp. 192–204. https://doi.org/10.2514/1.G000872.

[5] Christian, J. A., and Robinson, S. B., "Noniterative Horizon-Based Optical Navigation by Cholesky Factorization," *Journal of Guidance, Control, and Dynamics*, Vol. 39, No. 12, 2016, pp. 2757–2765. https://doi.org/10.2514/1.G000539.

[6] Franzese, V., Di Lizia, P., and Topputo, F., "Autonomous Optical Navigation for the Lunar Meteoroid Impacts Observer," *Journal of Guidance, Control, and Dynamics*, Vol. 42, No. 7, 2019, pp. 1579–1586. https://doi.org/10.2514/1.G003999.

[7] Nakath, D., Clemens, J., and Rachuy, C., "Active Asteroid-SLAM: Active Graph SLAM with Landing Site Discovery in a Deep Space Proximity Operations Scenario," *Journal of Intelligent & Robotic Systems*, Vol. 99, No. 2, 2020, pp. 303–333. https://doi.org/10.1007/s10846-019-01103-0.

[8] Kaluthantrige, A., Feng, J., and Gil-Fernández, J., "Convolutional-Neural-Network-Based Autonomous Navigation of Hera Mission Around Didymos," *Journal of Guidance, Control, and Dynamics*, Vol. 48, No. 1, 2025, pp. 46–59. https://doi.org/10.2514/1.G008054.

[9] Pugliatti, M., Piccolo, F., Rizza, A., Franzese, V., and Topputo, F., "The vision-based guidance, navigation, and control system of Hera's Milani Cubesat," *Acta Astronautica*, Vol. 210, 2023, pp. 14–28. https://doi.org/10.1016/j.actaastro.2023.04.047.

[10] Belgacem, I., Jonniaux, G., and Schmidt, F., "Image processing for precise geometry determination," *Planetary and Space Science*, Vol. 193, 2020, p. 105081. https://doi.org/10.1016/j.pss.2020.105081.

[11] Rufino, G., and Moccia, A., "Laboratory test system for performance evaluation of advanced star sensors," *Journal of Guidance, Control, and Dynamics*, Vol. 25, No. 2, 2002, pp. 200–208. https://doi.org/10.2514/2.4888.

[12] Boone, B. G., Bruzzi, J. R., Dellinger, W. F., Kluga, B. E., and Strobehn, K. M., "Optical simulator and testbed for spacecraft star tracker development," *Optical Modeling and Performance Predictions II*, Vol. 5867, edited by M. A. Kahan, International Society for Optics and Photonics, SPIE, 2005, p. 586711. https://doi.org/10.1117/12.619133.

[13] Rufino, G., Accardo, D., Grassi, M., Fasano, G., and Renga, U., A.and Tancredi, "Real-time hardware-in-the-loop tests of star tracker algorithms," *International Journal of Aerospace Engineering*, Vol. 2013, 2013, pp. 1–13. https://doi.org/10.1155/2013/505720.

[14] Samaan, M. A., Steffes, S. R., and Theil, S., "Star tracker real-time hardware in the loop testing using optical star simulator," *Proceedings of the 21st AAS/AIAA Space Flight Mechanics Meeting, New Orleans, USA*, Vol. 140, Univelt, Inc., P. O. Box 28130 San Diego CA 92198-0130 United States, 2011, pp. 2233—2245.

[15] Roessler, D., Pedersen, D. A. K., Benn, M., and Jørgensen, J. L., "Optical stimulator for vision-based sensors," *Advanced Optical Technologies*, Vol. 3, No. 2, 2014, pp. 199–207. https://doi.org/10.1515/aot-2013-0045.

[16] Beierle, C., Sullivan, J., and D'Amico, S., "Design and Utilization of the Stanford Vision-Based Navigation Testbed for Spacecraft Rendezvous," *Proceedings of the 9th International Workshop on Satellite Constellations and Formation Flying, University of Colorado Boulder, Boulder, CO, USA*, 2017, pp. 19–21.

[17] Filipe, N., Jones-Wilson, L., Mohan, S., Lo, K., and Jones-Wilson, W., "Miniaturized star tracker stimulator for closed-loop testing of cubesats," *Journal of Guidance, Control, and Dynamics*, Vol. 40, No. 12, 2017, pp. 3239–3246. https://doi.org/10.2514/1.G002794.

[18] Nardino, V., Guzzi, D., Burresi, M., Cecchi, M., Cecchi, T., Corti, F., Corti, M., Franci, E., Guidotti, G., Pippi, I., Salvadori, L., Spagnesi, C., and Raimondi, V., "MINISTAR: a miniaturized device for the test of star trackers," *International Conference on Space Optics—ICSO 2018*, Vol. 11180, SPIE, 2019, pp. 2821–2827.

[19] Beierle, C., and D'Amico, S., "Variable-magnification optical stimulator for training and validation of spaceborne vision-based navigation," *Journal of Spacecraft and Rockets*, Vol. 56, No. 4, 2019, pp. 1060–1072. https://doi.org/10.2514/1.a34337.

[20] Panicucci, P., and Topputo, F., "The TinyV3RSE Hardware-in-the-Loop Vision-Based Navigation Facility," *Sensors*, Vol. 22, No. 23, 2022, p. 9333. https://doi.org/10.3390/s22239333.

[21] Panicucci, P., Ornati, F., and Topputo, F., "Design of a Low-Aberration Variable-Magnification Optical Stimulator for Vision System Hardware-in-The-Loop Testing," *IEEE Transactions on Aerospace and Electronic Systems*, 2025, pp. 1–22. https://doi.org/10.1109/TAES.2025.3580393.

[22] Di Domenico, G., Andreis, E., Morelli, A. C., Merisio, G., Franzese, V., Giordano, C., Morselli, A., Panicucci, P., Ferrari, F., and Topputo, F., "The ERC-Funded EXTREMA Project: Achieving Self-Driving Interplanetary CubeSats," *Modeling and Optimization in Space Engineering: New Concepts and Approaches*, Springer, 2022, pp. 167–199. https://doi.org/10.1007/978-3-031-24812-2_6.

[23] Di Domenico, G., Perico, D., Ornati, F., Giordano, C., Morselli, A., Panicucci, P., and Topputo, F., "The EXTREMA Simulation Hub: Advancements in the Development of an Integrated Hardware-In-the-loop Facility for Autonomous Cubesats GNC Technologies," *4S Symposium*, 2024, pp. 1–22.

[24] Andreis, E., Panicucci, P., Ornati, F., Perico, D., Topputo, F., et al., "Autonomous Vision-Based Navigation for Deep-Space CubeSats: Algorithm Development and Hardware Validation," *75th International Astronautical Congress (IAC 2024)*, 2024, pp. 1–11.

[25] Kruger, J., Koenig, A. W., and D'Amico, S., "Starling Formation-Flying Optical Experiment (StarFOX): System Design and Preflight Verification," *Journal of Spacecraft and Rockets*, Vol. 60, No. 6, 2023, pp. 1755–1777. https://doi.org/10.2514/1.A35598.

[26] Gaias, G., and Ardaens, J.-S., "Flight Demonstration of Autonomous Noncooperative Rendezvous in Low Earth Orbit," *Journal of Guidance, Control, and Dynamics*, Vol. 41, No. 6, 2018, pp. 1337–1354. https://doi.org/10.2514/1.G003239.

[27] Kobylka, K. R., "Camera Exposure Time Determination for Artemis I Lunar Flyby," *4th Space Imaging Workshop*, 2024, pp. 1–5.

[28] McCluney, W. R., *Introduction to radiometry and photometry*, Artech House, 2014.

[29] Gardner, R., and Verghese, K., "On the solid angle subtended by a circular disc," *Nuclear Instruments and Methods*, Vol. 93, No. 1, 1971, pp. 163–167. https://doi.org/10.1016/0029-554X(71)90155-8.

[30] Scholz, S., Kondakov, D., Lüssem, B., and Leo, K., "Degradation Mechanisms and Reactions in Organic Light-Emitting Devices," *Chemical Reviews*, Vol. 115, No. 16, 2015, pp. 8449–8503. https://doi.org/10.1021/cr400704v.

[31] International Commission on Illumination, *Colorimetry – Part 1: CIE Standard Colorimetric Observers*, 4^{th} ed., CIE 015:2018, CIE, Vienna, Austria, 2018.

[32] Schanda, J., *Colorimetry: Understanding the CIE system*, John Wiley & Sons Press, 2007.

[33] Wyszecki, G., and Stiles, W. S., *Color science: concepts and methods, quantitative data and formulae*, John Wiley & sons, 2000.

[34] Bessell, M., "UBVRI passbands." *Publications of the Astronomical Society of the Pacific*, Vol. 102, No. 656, 1990, p. 1181. https://doi.org/10.1086/132749.

[35] Perryman, M. A., Lindegren, L., Kovalevsky, J., Hoeg, E., Bastian, U., Bernacca, P., Crézé, M., Donati, F., Grenon, M., Grewing, M., et al., "The HIPPARCOS catalogue," *Astronomy and Astrophysics*, Vol. 323, 1997, pp. L49–L52.

[36] Høg, E., "Tycho Star Catalogs: The 2.5 Million Brightest Stars," *Encyclopedia of Astronomy & Astrophysics*, CRC Press, 2001, pp. 1–3.

[37] Ballesteros, F., "New insights into black bodies," *Europhysics Letters*, Vol. 97, No. 3, 2012, p. 34008. https://doi.org/10.1209/0295-5075/97/34008.

[38] Sekiguchi, M., and Fukugita, M., "A Study of the B- V Color-Temperature Relation," *The Astronomical Journal*, Vol. 120, No. 2, 2000, p. 1072. https://doi.org/10.1086/301490.

[39] Mallama, A., and Hilton, J. L., "Computing apparent planetary magnitudes for The Astronomical Almanac," *Astronomy and computing*, Vol. 25, 2018, pp. 10–24. https://doi.org/10.1016/j.ascom.2018.08.002.

[40] Muller, G., "Number 30. Achten Bandes Viertes Stuck. Helligkeitsbestimmungen der grossen planeten und einiger asteroiden." *Publikationen des Astrophysikalischen Observatoriums zu Potsdam, Vol. 8, p. 193-389*, Vol. 8, 1893, pp. 193–389.

[41] Villanueva, G. L., Smith, M. D., Protopapa, S., Faggi, S., and Mandell, A. M., "Planetary Spectrum Generator: An accurate online radiative transfer suite for atmospheres, comets, small bodies and exoplanets," *Journal of Quantitative Spectroscopy and Radiative Transfer*, Vol. 217, 2018, pp. 86–104. https://doi.org/10.1016/j.jqsrt.2018.05.023.

[42] Lebreton, J., Brochard, R., Baudry, M., Jonniaux, G., Salah, A. H., Kanani, K., Le Goff, M., Masson, A., Ollagnier, N., Panicucci, P., Proag, A., and Robin, C., "Image Simulation for Space Applications with the SurRender Software," *Proceedings of the 11th International ESA Conference on Guidance, Navigation & Control Systems, 22 - 25 June 2021, Virtual*, 2021, pp. 1–16.

[43] Rowell, N., Parkes, S., Dunstan, M., and Dubois-Matra, O., "PANGU: Virtual spacecraft image generation," *5th International Conference on Astrodynamics Tools and Techniques, ICATT*, 2012, pp. L49–L52.

[44] Pugliatti, M., Buonagura, C., and Topputo, F., "CORTO: The Celestial Object Rendering TOol at DART Lab," *Sensors*, Vol. 23, No. 23, 2023. https://doi.org/10.3390/s23239595.

[45] Pizzetti, A., Panicucci, P., and Topputo, F., "A Radiometric Consistent Render Procedure for Planets and Moons," *4th Space Imaging Workshop*, 2024, pp. 1–3.

[46] Pizzetti, A., Panicucci, P., Capolupo, F., and Topputo, F., "Development and Validation of a Physically Based Rendering Methodology for Celestial Bodies," *Acta Astronautica*, 2025. Under review.

[47] Morresi, M., Bettarini, R., Procopio, D., and Berrighi, G., "AA-STR MKII: Developing a Next Generation Autonomous Star Sensor," *Proceedings of the 44th Annual American Astronautical Society Guidance, Navigation, and Control Conference, 2022*, edited by M. Sandnas and D. B. Spencer, Springer International Publishing, Cham, 2024, pp. 233–234. https://doi.org/10.1007/978-3-031-51928-4_15.

[48] Panicucci, P., Balossi, C., Ornati, F., Piccolo, F., Pizzetti, A., Topputo, F., and Capolupo, F., "What if Star Trackers Were Navigation Cameras?" *35th AAS/AIAA Space Flight Mechanics Meeting, Kaua'i, Hawaii*, 2025, pp. 1–23.

[49] Balossi, C., Piccolo, F., Panicucci, P., Pugliatti, M., Topputo, F., and Capolupo, F., "Moon Limb-Based Autonomous Optical Navigation Using Star Trackers," *46th AAS Guidance, Navigation and Control Conference*, 2024, pp. 1–19.

[50] Piccolo, F., Balossi, C., Panicucci, P., Pugliatti, M., Topputo, F., and Capolupo, F., "Resource-Constrained Vision-Based Relative Navigation About Small Bodies," *46th AAS Guidance, Navigation and Control Conference*, 2024, pp. 1–18.

[51] Pizzetti, A., Ornati, F., Balossi, C., Piccolo, F., Panicucci, P., Topputo, F., Capolupo, F., and Casasco, M., "The STAR Nav Moon Dataset," , April 2025. https://doi.org/10.5281/zenodo.15166001.

[52] Hartmann, P., "110 years BK7: optical glass type with long tradition and ongoing progress," *Optical Systems Design 2012*, Vol. 8550, International Society for Optics and Photonics, SPIE, 2012, p. 85500U. https://doi.org/10.1117/12.981784.

[53] Regnier, P., and Grzymisch, J., "JUICENA Guidance Navigation & Control Sub-System: overall in-flight performance and Vision-Based Navigation on-ground validation," *46th Annual AAS Guidance, Navigation and Control Conference*, 2024.

[54] Nakamura, J., *Image sensors and signal processing for digital still cameras*, CRC press, 2017.

[55] Belloir, J.-M., Lincelles, J.-B., Pelamatti, A., Durnez, C., Goiffon, V., Virmontois, C., Paillet, P., Magnan, P., and Gilardx, O., "Dark current blooming in pinned photodiode CMOS image sensors," *IEEE Transactions on Electron Devices*, Vol. 64, No. 3, 2017, pp. 1161–1166. https://doi.org/10.1109/TED.2017.2654515.

[56] Wang, Z., Bovik, A. C., Sheikh, H. R., and Simoncelli, E. P., "Image quality assessment: from error visibility to structural similarity," *IEEE transactions on image processing*, Vol. 13, No. 4, 2004, pp. 600–612. https://doi.org/10.1109/TIP.2003.819861.

[57] Acton, C., Bachman, N., Elson, L., Semenov, B., Turner, F., and Wright, E., "Extending NASA's SPICE ancillary information system to meet future mission needs," *SpaceOps 2002 Conference*, 2005, p. 9.

[58] Geary, J. M., *Introduction to lens design: with practical ZEMAX examples*, Willmann-Bell Richmond, VA, USA, 2002.

[59] Horvath, H., "Atmospheric light absorption—A review," *Atmospheric Environment. Part A. General Topics*, Vol. 27, No. 3, 1993, pp. 293–317. https://doi.org/10.1016/0960-1686(93)90104-7.